Linearization Angle Widened Digital Predistortion for 5G MIMO Beamforming Transmitters

Qing Luo, *Graduate Student Member, IEEE*, Xiao-Wei Zhu, *Member, IEEE*,
Chao Yu, *Senior Member, IEEE*, Dan-Dan Teng, *Student Member, IEEE*,
Xiaoyu Wang, *Graduate Student Member, IEEE*, Chenhao Chu, *Graduate Student Member, IEEE*,
Wei Hong, *Fellow, IEEE*, and Anding Zhu, *Senior Member, IEEE*

Abstract— To reduce the demand for frequently adjusting phase shifts in the fifth-generation (5G) multiple-input multiple-output (MIMO) beamforming transmitters, in this article, a novel digital predistortion (DPD) technique is proposed, which employs multiple predistortion boxes to shape the pattern of nonlinear distortions in space in order to linearize multiple targets simultaneously. By using this approach, the linearization angle is widened and thus the communication quality can be kept when the user moves off the main beam direction. As a proof of concept, two DPD boxes, namely main and auxiliary boxes, are used to realize the 2-target linearization. A new model extraction method is also proposed with a dedicated over-the-air (OTA) feedback post-processing stage. Simulation and experiment are demonstrated on a 4-path beamforming transmitter. The results show that the proposed DPD method can effectively widen the linearization angle with reasonable additional complexity.

Index Terms— Beamforming, behavioral modeling, digital predistortion (DPD), multiple-input multiple-output (MIMO), power amplifier (PA) linearization.

I. INTRODUCTION

TO IMPROVE power efficiency and enhance spectrum utilization, beamforming and multiple-input multiple-output (MIMO) techniques are employed in the fifth-generation (5G) wireless systems [1]. Compared with single-antenna systems, the average power of each transmitter path is lower in MIMO systems, but the power amplifier (PA) still dominates the power consumption in wireless communication [2]. Although many techniques have been developed to improve efficiency or linearity, tradeoff between efficiency and linearity is still crucial in radio frequency (RF) design.

Digital predistortion (DPD) has been widely deployed to guarantee linearity of the PAs operating in the high-efficiency
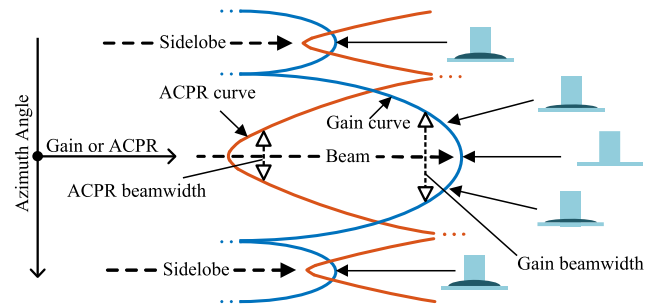
Fig. 1. Typical gain and linearization performance of BO-DPD.

mode [3], [4]. To date, most DPD techniques are developed for linearizing single-input single-output (SISO) systems. They encounter difficulties in MIMO systems, especially in those with analog or hybrid beamforming architectures where it is not feasible to deploy separate DPD for each RF chain.

In the past years, research on DPD for MIMO systems has been mainly focusing on model development, crosstalk cancellation, and feedback data acquisition techniques [5], [6], such as dual-input models [7]–[9], neural network models [10], single-receiver over-the-air (OTA) DPD [11], and the indirect identification method with OTA tests [12]. At the architecture level, two main MIMO DPD schemes have been proposed: beam-oriented (BO) DPD [13], [14] and full-angle DPD [15].

The BO-DPD is a single-target linearization approach in which the signal received at the main beam direction is treated as the reference and the conventional SISO DPD model is used to linearize the transmitter [14], [16]. The typical performance of BO-DPD is illustrated in Fig. 1. In a real system, the PAs at different branches may behave differently because of fabrication and operation variations. Due to the inconsistency between PAs, this BO-DPD can only guarantee the linearity at the reference direction. In other directions, the nonlinearity or out-of-band (OOB) emission is inevitable and thus the adjacent channel power ratio (ACPR) is degraded when the user is off the beam direction.

According to the analysis of spatial nonlinear leakage [14], and the simulations of OOB emission [12], [17], the nonlinearity emission may not cause a serious problem in all directions, e.g., in the sidelobe, the distortion may be tolerable since the

transmission power is low. However, OOB emission can limit the main beam range. Due to the directional nonlinearity emission, the ACPR usually deteriorates faster than the decrease of the array gain in the beam if only one linearization direction is considered. In other words, the ACPR curve is steeper than the gain curve, as illustrated in Fig. 1. Comparing the two curves, we can see that 3-dB ACPR beamwidth is narrower than 3-dB gain beamwidth. Under such circumstances, the user may still receive strong enough signals when it is off the main beam direction but the linearity will deteriorate. Therefore, if the linearity is considered as a limiting factor, the available moving range of the user will be narrowed. This leads that, when the user moves off the main beam direction, we have to either adjust the beam steering angle by changing the phase shift in the transmitter or re-calibrate the DPD to recover the linearity loss. This is not desirable in the real-time system operation since frequently changing beam steering angle or re-calibrating DPD will significantly increase power consumption and system operation cost. For instance, finding the correct adjustment to point the beam to the exact new direction would need accurate channel estimation that involves complicated signal processing. Keeping high precision beam steering is also difficult in some cases, such as the unmanned aerial vehicle (UAV)-based networks where the base stations on the air cannot be kept steady due to vibration [18].

In the full-angle DPD [15], the variations of the PA in different transmitter chains are compensated with tuning boxes first and then a common DPD block is adopted to linearize the whole subarray. Based on this operation, all the transmitter chains can be effectively linearized simultaneously, and thus the signals at all directions become linear. Because one-to-one mappings must be found between the PAs and the cascade boxes, the system complexity can be high by using this full-angle DPD in a large array where tens or hundreds of RF chains are involved. Furthermore, in hybrid beamforming, accurate analog tuning is difficult.

In this article, we propose a multi-target DPD approach that can extend the linearization range of the beamforming transmitters without significantly increasing the system complexity. As a demonstration, a 2-target DPD system is implemented, that can significantly extend the linearization angle of the transmitter so that the communication quality can be kept when the user moves off the main-beam direction. This reduces the demand for frequently adjusting phase shifts in the beamforming transmitter or re-calibrating DPD. This is achieved by adding a low-power auxiliary DPD output with additional phase-shifts to RF chains to manipulate nonlinear distortion distribution. An OTA signal post-processing technique is also developed to fit the indirect learning architecture (ILA) in model extraction. The proposed system is well suitable for a large-scale MIMO array.

The rest of the article is arranged as follows. Section II introduces the new multi-target DPD architecture. Section III presents the detailed model extraction. Section IV validates the proposed DPD by simulating MIMO transmitters. In Section V, experimental results are provided and explained, with a conclusion given in Section VI.
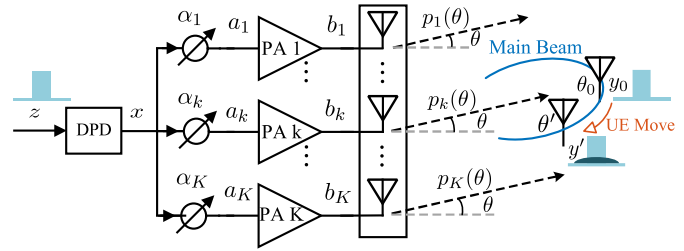

Fig. 2. Block diagram of a beamforming system.

II. ARCHITECTURE OF MULTI-TARGET DPD

In this section, a new DPD architecture is derived to achieve multi-target linearization, and thus the linearization angle of the MIMO transmitter can be widened, so that there is no need to adjust phase shifts in the transmitting chains when the user moves off the main beam direction within a certain range.

For simplicity, we consider a uniform linear array (ULA) consisting of K active antennas with equal half-wavelength spacing, as shown in Fig. 2. The beam direction of the MIMO transmitters is controlled by phase shifting weights $\alpha_k = \phi(k - 1)$ in the phase shifters. The amplitude weights in the RF chains are assumed to be 1. One DPD block is assumed to linearize the entire array and all the signals are in baseband equivalent format. To simplify analysis, antenna crosstalk is not considered in the model derivation but the impact of crosstalk is simulated in Section IV.

A. System Model and Existing DPD

Let us assume the original input signal is z and the DPD output signal is x. The input and output of the PAs are a_k and b_k, respectively, where k is the index of the PA, and

$$b_k = R^{(k)}[a_k] \tag{1}$$

where $R^{(k)}[\cdot]$ represents the nonlinear function of the PA. The output of DPD x is phase-shifted by the phase shifters before entering PA. In the general RF PA system, we can assume there is no phase modulation to amplitude modulation (PM-AM) or phase modulation to phase modulation (PM-PM) distortion. Therefore, the phase-shifts can be moved out of the nonlinear function and thus the output of the PA can be expressed as

$$b_k = R^{(k)}[xe^{j\phi(k-1)}] = R^{(k)}[x]e^{j\phi(k-1)}. \tag{2}$$

The output of the PA will be radiated to the air and received by the user equipment (UE). The far-field transmitted signal in the direction angle θ is

$$y(\theta) = \sum_{k=1}^{K}\{R^{(k)}[x]e^{j\phi(k-1)}p_k(\theta)\} \tag{3}$$

where $p_k(\theta) = e^{-j\pi \sin(\theta\pi/180)(k-1)}$ represents the phase shift in the propagation channel.

To maximize the received signal in the main-beam direction θ_0, the phase shifters in the transmitter need compensate the phase shifts caused by the channel as

$$e^{j\phi(k-1)}p_k(\theta_0) = e^{j0} = 1 \tag{4}$$
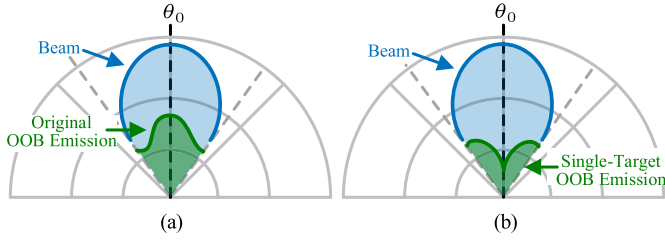
which means that $\phi = \pi \sin(\theta_0\pi/180)$.

Fig. 3. (a) Diagram of the beam and the OOB emission pattern without DPD. (b) Diagram of the single-target OOB emission pattern.
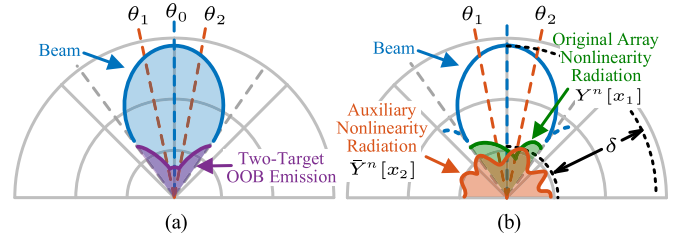

Fig. 4. (a) Diagram of the 2-target OOB emission pattern. (b) Diagram of the original and auxiliary nonlinearity radiation patterns of the proposed DPD.

In this case, all the signals are in-phase at the receiver direction and therefore the received signal $y(\theta_0)$ in the main beam direction θ_0, defined as y_0, becomes the sum of the PA outputs $R^{(k)}[x]$ as

$$y_0 = \sum_{k=1}^{K} R^{(k)}[x]. \tag{5}$$

In the BO-DPD scheme [14], the main beam signal y_0 is used as the reference signal and thus with DPD, y_0 will be equal to the original input signal, namely

$$y_0 = \sum_{k=1}^{K} R^{(k)}[x] = z \tag{6}$$

assuming all the signals are normalized.

As shown in Fig. 3(a), the transmitter power pattern is oriented at θ_0, and without DPD, the OOB emission pattern basically follows the beam pattern. With DPD, the OOB emission in the main beam direction is reduced but at other directions it remains, as shown in Fig. 3(b). This is because, in other directions, e.g., θ', the received signal y' will be a sum of phase-shifted $R^{(k)}[x]$ as

$$y' = \sum_{k=1}^{K} \{R^{(k)}[x]e^{j\phi(k-1)}p_k(\theta')\} \tag{7}$$

where

$$e^{j\phi(k-1)}p_k(\theta') \neq 1. \tag{8}$$

In the real system, due to variations in the fabrication process and in the RF chain settings, the PAs at different RF chains may behave differently, e.g., $R^{(1)}[x] \neq R^{(2)}[x]$. This results that the sum of phase-shifted $R^{(k)}[x]$, y' cannot be linear version of z, even if the direct sum of $R^{(k)}[x]$ is z.

In [15], the full-angle DPD uses tuning boxes to make the PAs in different transmitter chains behavior the same, and then a common DPD block is adopted to linearize the whole subarray. Based on this operation, the distortions at different angles can be effectively linearized simultaneously, but the system complexity can be high if a large number of RF chains are involved.

B. Multi-Target DPD

Due to the distortion not being canceled out in the non-main beam directions, the BO-DPD will have a narrow nulling OOB emission pattern. In this case, the moving range of the user

will be limited since the distortion will rise quickly if the user is off the main beam. In practice, it is desirable to have a wider linearization range, such as the scenario shown in Fig. 4(a), where the distortions within the range of θ_1 to θ_2 are kept low so that the user can move within that range without losing linearity.

To achieve the scenario shown in Fig. 4(a), a multi-target DPD solution is required. In other words, we need to simultaneously linearize multiple directions within the range of θ_1 and θ_2. For a proof of concept, we use a 2-target DPD system as an example. First, the original beamforming direction shall not be changed, namely, the phase-shifts in the transmitter are set to point the beam to the main beam direction, which means that $\phi = \pi \sin(\theta_0\pi/180)$. Different from the BO-DPD, in the new scenario, we use the outputs at θ_1 and θ_2 as the reference signals, namely, we would desire the two equations below to be satisfied

$$\begin{cases} y_1 = \sum_{k=1}^{K} \{R^{(k)}[x]e^{j\phi(k-1)}p_k(\theta_1)\} = z \\ y_2 = \sum_{k=1}^{K} \{R^{(k)}[x]e^{j\phi(k-1)}p_k(\theta_2)\} = z. \end{cases} \tag{9}$$

This, however, is not possible, since the phase shift differences between θ_1 and θ_2 result in different nonlinearities in two directions, and thus y_1 cannot be equal to y_2 at the same time.

To simultaneously linearize two directions, we can add an additional input passing through another nonlinear model to generate an auxiliary nonlinearity, as shown in Fig. 4(b). The distortion in both directions can then be compensated.

To facilitate derivation, we use $Y^{(n)}$ to represent the transfer function of the existing transmitter, where n is the index of beam angle and x_1 is the input, namely

$$Y^{(n)}[x_1] = \sum_{k=1}^{K} \{R^{(k)}[x_1]e^{j\phi(k-1)}p_k(\theta_n)\} \tag{10}$$

and we use $\bar{Y}^{(n)}$ to represent the new function with input x_2.

Equation (9) becomes

$$\begin{cases} y_1 = Y^{(1)}[x_1] + \bar{Y}^{(1)}[x_2] = z \\ y_2 = Y^{(2)}[x_1] + \bar{Y}^{(2)}[x_2] = z \end{cases} \tag{11}$$

where x_2 can be generated from x_1 by using a predistortion model D as
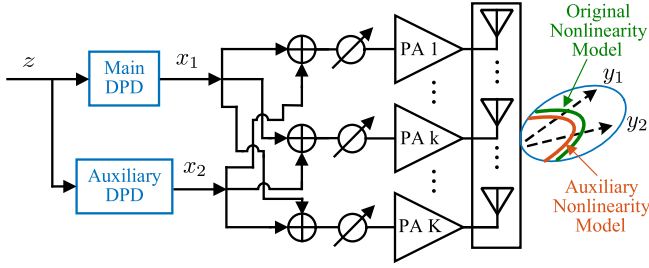
$$x_2 = D[x_1]. \tag{12}$$

Fig. 5. Block diagram of the predistortion structure with two DPD outputs sharing the same transmitting chains.

Fig. 6. Block diagram of the proposed DPD.

Substituting (12) in (11), we obtain

$$Y^{(1)}[x_1] + \bar{Y}^{(1)}[D[x_1]] = Y^{(2)}[x_1] + \bar{Y}^{(2)}[D[x_1]] \quad (13)$$

which can be rewritten for simplicity as

$$Y^{(1)} + \bar{Y}^{(1)}D = Y^{(2)} + \bar{Y}^{(2)}D. \quad (14)$$

Since $Y^{(1)} \neq Y^{(2)}$ and $\bar{Y}^{(1)} \neq \bar{Y}^{(2)}$, the model D can be obtained as

$$D = -(\bar{Y}^{(1)} - \bar{Y}^{(2)})^{-1}(Y^{(1)} - Y^{(2)}). \quad (15)$$

From (15), we can see that if $\bar{Y}^{(n)} = Y^{(n)}$, D will be a simple negative function, which leads

$$x_2 = -x_1. \quad (16)$$

This will result in $z = 0$ in (11), which is meaningless. This is illustrated in Fig. 5, if x_2 passes the transmitter array in the same way as that of x_1, the two-box predistortion structure will degenerate into a single-box scheme, which cannot simultaneously linearize two directions. This conclusion also indicates that using averaged outputs cross multiple directions as the reference to extend the linearization angle, as conducted in [14], is not an optimum solution.

Therefore, to satisfy (11), we must have

$$\bar{Y}^{(n)} \neq Y^{(n)}. \quad (17)$$

The question now is, how we can construct a different nonlinear function in the MIMO transmitter. After extensive search, we found a very simple way to do this. As discussed earlier, summing up phase-shifted PA outputs would generate nonlinearity, as shown in (7). Using this property, we can construct the auxiliary nonlinear model $\bar{Y}^{(n)}$ by simply introducing phase shift γ_k to the PA inputs in the array as

$$\bar{Y}^{(n)}[x_2] = \sum_{k=1}^{K} \{R^{(k)}[e^{-j\gamma_k}x_2]e^{j\phi(k-1)}p_k(\theta_n)\}. \quad (18)$$

Interestingly, γ_k can be arbitrarily chosen as long as it does not lead to the output of the auxiliary model overlapping with that of the original transmitter model $Y^{(n)}$. And it is not necessary to add γ_k to all the branches. A minimum one γ_k is required for a 2-target DPD.

In the real operation, x_1 and x_2 must pass the same MIMO transmitter at the same time. Considering x_2 is mainly used to compensate the additional distortion caused by beam offset, the power of x_2 can be kept relatively small. We thus introduce
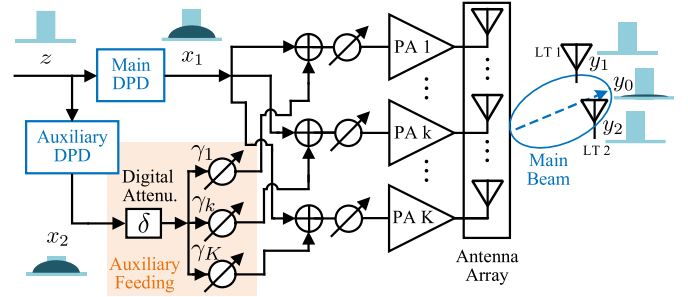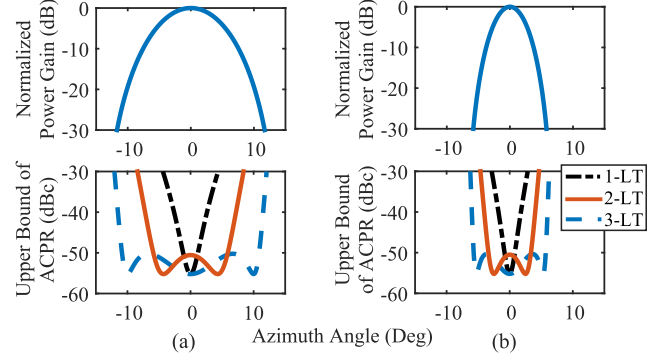

Fig. 7. Normalized beam pattern and ACPR distributions with multiple linearization targets for (a) 8-antenna array and (b) 16-antenna array.

a scaling factor δ for x_2. The x_1 and x_2 can then be combined in the input and the 2-target equations of (11) can be converted to

$$\begin{cases} y_1 = \sum_{k=1}^{K} \{R^{(k)}[x_1 + e^{-j\gamma_k}\delta x_2]e^{j\phi(k-1)}p_k(\theta_1)\} = z \\ y_2 = \sum_{k=1}^{K} \{R^{(k)}[x_1 + e^{-j\gamma_k}\delta x_2]e^{j\phi(k-1)}p_k(\theta_2)\} = z. \end{cases} \quad (19)$$

The proposed DPD system can be implemented by using the architecture illustrated in Fig. 6, where the main DPD box and the auxiliary DPD box are employed in parallel to predistort the same input signal z. The power of the main DPD output x_1 is kept at a normal level. The auxiliary DPD output x_2 may be highly nonlinear but scaled by δ to relatively lower power, and x_2 is phase-shifted by γ_k before being combined with x_1. In a fully digital system, γ_k can be easily added in the digital domain while in hybrid or analog beamforming, analog phase-shifters or butler matrix can be used [19], [20].

If more targets are set, more auxiliary nonlinear models can be added accordingly and the linearization angle may be widened further. For illustration, the beam patterns and corresponding ACPR upper bound for different size arrays are given in Fig. 7(a) and (b), where the noise floor is assumed to be about -55 dBc. For the 8-antenna linear array, the target angles are $0°$ for 1-LT, $-4.3°, 4.3°$ for 2-LT, $-10°, 0°$, and $10°$ for 3-LT, where LT stands for "Linearization Target." For the 16-antenna linear array, the target angles are $0°$ for 1-LT, $-2.5°, 2.5°$ for 2-LT, $-5.3°, 0°, 5.3°$ for 3-LT. It can be observed that the wider ACPR beamwidth can be achieved

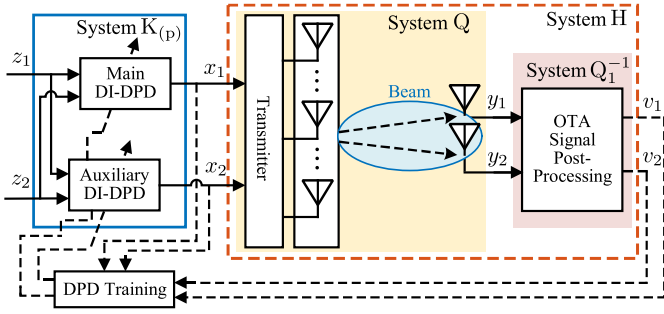Fig. 8.   Block diagram of the proposed DPD model extraction structure.

Fig. 9.   (a) Cascade connection of system $K_{(p)}$, system Q and system Q_1^{-1}. (b) Cascade connection of system Q, system Q_1^{-1}, and system $K_{(p)}$.

with more linearization targets. Comparing the gain and ACPR curves, they are scaled accordingly. Such results reveal that the proposed multi-target DPD performs well for large-scale MIMO transmitters.

III. MODEL EXTRACTION

In the proposed system, two DPD boxes are used. To facilitate model extraction, we can treat the system as a dual-input dual-output system, as shown in Fig. 8. The conventional dual-input DPD (DI-DPD) models can be directly deployed. Two signals, z_1 and z_2, are used in the input and two outputs, y_1 and y_2, are captured via OTA measurements, e.g., OTA diversity feedbacks [21]. Alternative methods, including coupler-based combined feedback [22], embedded antennas [23], [24], and common feedback line [25], can be used as well.

The reason to use dual-input-dual-output system is to use the ILA architecture for model extraction. According to the theory of pth-order inverse of MIMO nonlinear system [26], the pth-order pre-inverse and post-inverse of system H are the same and the inverse system can be uniquely identified. This means that the pth-order pre-inverse can be identified by determining the pth-order post-inverse, as the ILA does.

A. OTA Signal Post-Processing

Different from the conventional dual-input-dual-output system is that, in this system, we only require the outputs to be linear versions of inputs. In other words, we do not require $y_1 = z_1$ or $y_2 = z_2$ but $y_1 = a * z_1 + b * z_2$, where a and b are scaling factors, since z_1 and z_2 will be the same after model extraction. Taking advantage of this property, we add an OTA signal post-processing box to decouple y_1 and y_2 into two separate signals v_1, v_2 before model extraction.

The linear post-processing can be described as

$$\begin{bmatrix} \mathbf{v}_1 \\ \mathbf{v}_2 \end{bmatrix} = \mathbf{Q}_1^{-1} \begin{bmatrix} \mathbf{y}_1 \\ \mathbf{y}_2 \end{bmatrix} \tag{20}$$

where $\mathbf{y}_k = [y_k(1), \ldots, y_k(N)]$, $\mathbf{v}_k = [v_k(1), \ldots, v_k(N)]$ are the signal vectors with all the samples, matrix $\mathbf{Q}_1^{-1}$ represents the inverse of the linear part of system Q.

As shown in Fig. 9(a), the system is transformed to a cascade connection of DPD system $K_{(p)}$, Q and Q_1^{-1}, where $K_{(p)}$ needs to be determined as the pre-inverse of the system H.
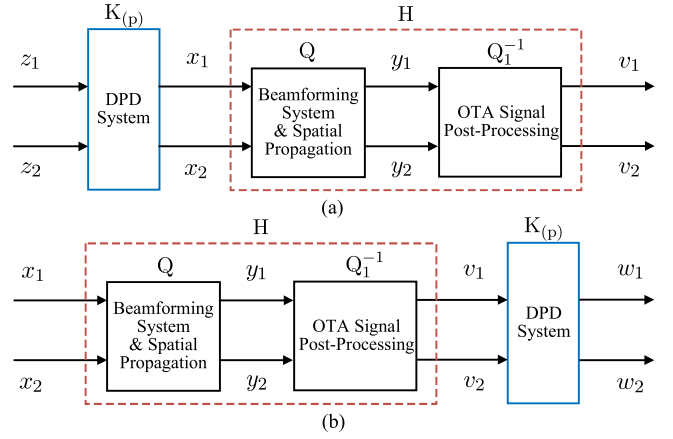
Once $\mathbf{v}_1$ and $\mathbf{v}_2$ have been linearized to $\mathbf{z}_1$ and $\mathbf{z}_2$, because $\mathbf{Q}_1$ is the inverse matrix of $\mathbf{Q}_1^{-1}$, from (20), $\mathbf{y}_1$ and $\mathbf{y}_2$ will be given as

$$\begin{bmatrix} \mathbf{y}_1 \\ \mathbf{y}_2 \end{bmatrix} = \mathbf{Q}_1 \begin{bmatrix} \mathbf{v}_1 \\ \mathbf{v}_2 \end{bmatrix} = \mathbf{Q}_1 \begin{bmatrix} \mathbf{z}_1 \\ \mathbf{z}_2 \end{bmatrix} \tag{21}$$

where y_1 and y_2 will also be already linear.

The feeding network, the PA linear gains, and the OTA phase shifts are known or can be measured. In our proposed DPD, the matrix $\mathbf{Q}_1$ or its inverse matrix $\mathbf{Q}_1^{-1}$ could be estimated directly. Least-square (LS) method is used to resolve regression equations as

$$\mathbf{Q}_1^{-1} = \begin{bmatrix} \mathbf{x}_1 \\ \mathbf{x}_2 \end{bmatrix} \mathbf{Y}^{\dagger} \tag{22}$$

where $\mathbf{x}_k = [x_k(1), \ldots, x_k(N)]$ is a signal vector with all the samples. $\mathbf{Y} = [\mathbf{y}_1^T \ \mathbf{y}_2^T]^T$, and $\mathbf{Y}^{\dagger}$ is the pseudo-inverse of $\mathbf{Y}$, as $\mathbf{Y}^{\dagger} = \mathbf{Y}^H (\mathbf{Y}^H \mathbf{Y})^{-1}$ when $\mathbf{Y}$ is a row full rank matrix.

B. Model Extraction

Since the post-processing Q_1^{-1} is added, the pre-inverse $K_{(p)}$ of system H can be determined by ILA as a post-inverse, as shown in Fig. 9(b). The outputs of $K_{(p)}$ as a post-inverse should be $\mathbf{w}_1 = \mathbf{x}_1$ and $\mathbf{w}_2 = \mathbf{x}_2$, where $\mathbf{w}_k = [w_k(1), \ldots, w_k(N)]$.

In practice, the dual-input-dual-output block of $K_{(p)}$ is divided into two DI-DPD models. Existing nonlinear models with an appropriate pruning of bivariate Volterra series, such as the extended generalized memory polynomial for nonlinear crosstalk (EGMPNLC) model in [27], can be used as the DI-DPD models, which are given as

$$\begin{bmatrix} \mathbf{x}_1^T & \mathbf{x}_2^T \end{bmatrix} = \mathbf{F}(\mathbf{z}_1, \mathbf{z}_2) \begin{bmatrix} \mathbf{c}_1 & \mathbf{c}_2 \end{bmatrix} \tag{23}$$

where $\mathbf{c}_1, \mathbf{c}_2$ are the coefficient column vectors of the main and auxiliary DI-DPD models, the term matrix $\mathbf{F}(\mathbf{z}_1, \mathbf{z}_2)$ is

$$\mathbf{F}(\mathbf{z}_1, \mathbf{z}_2) = \begin{bmatrix} \mathbf{f}(z_1(1), z_2(1)) \\ \vdots \\ \mathbf{f}(z_1(N), z_2(N)) \end{bmatrix} \tag{24}$$

where the row vector $\mathbf{f}(z_1(1), z_2(1))$ contains the basic functions of the DI-DPD model.

Then the coefficients of the main DI-DPD and the auxiliary DI-DPD can be determined by LS algorithm as

$$[\mathbf{c}_1 \quad \mathbf{c}_2] = \mathbf{F}(\mathbf{v}_1, \mathbf{v}_2)^\dagger [\mathbf{x}_1^T \quad \mathbf{x}_2^T] \qquad (25)$$

where $\mathbf{F}(\mathbf{v}_1, \mathbf{v}_2)^\dagger$ is the pseudo-inverse of $\mathbf{F}(\mathbf{v}_1, \mathbf{v}_2)$, as $\mathbf{F}^\dagger = (\mathbf{F}^H \mathbf{F})^{-1} \mathbf{F}^H$ when $\mathbf{F}$ is a column full rank matrix.

C. Model Combining

After the DI-DPD model extraction, both the main input z_1 and auxiliary input signal z_2 will be replaced with the original signal z, the bivariate model $K_{(p)}$ will be transformed directly to two conventional univariate models, e.g., the generalized memory polynomial (GMP) model [28], as the main and auxiliary DPD models in Fig. 6. The number of coefficients will be reduced to be less than half compared with that of the extraction models. The linear transformation from the bivariate-model coefficient vectors to univariate-model coefficient vectors can be conducted by using matrix manipulation depending on the DI-DPD model chosen.

IV. SIMULATION RESULTS

In this section, the performance of the proposed DPD technique is validated with simulation. A 4-path transmitter with omnidirectional antennas was simulated first, and 8- and 16-path transmitters were then simulated to validate the large-scale adaptability. The antenna array spacing is half-wavelength and the feedback was captured via OTA in far-field. Two 20-MHz orthogonal frequency-division multiplexing (OFDM) signals were used and the peak-to-average power ratios (PAPRs) are around 6.5 dB. The maximum of the PA input was normalized to be 1 in the simulation, and the PA model coefficients were extracted from real MOSFET PAs operating at 1.93 GHz. The nonlinearity and memory effects were set differently in each path to emulate the variations among paths. Additive white Gaussian noise was added at the PA output. The EGMPNLC model was used in model extraction and the GMP model was employed in the final DPD. Both models used the same settings with $P = 7$, $M_1 = 5$, and $M_2 = 1$.

A. Linearization Performance Comparison

For comparison, we simulated the 4-path transmitter with BO-DPD and the proposed DPD. In BO-DPD, the reference signal was captured at 0°, while in the proposed DPD, the signals at ±13° were used. $\delta = -25.6$ dB and $\gamma_k = -\pi \sin(20\pi/180)(k-1)$ where $k = 1$ to 4. The ACPR and normalized mean square error (NMSE) values are given in Table I, where y_0 is the main beam signal at 0°, y_1, y_2 are the two target signals at −13° and +13°, respectively. The corresponding power spectral density (PSD) for the received signals after DPD are shown in Fig. 10. From the results, we can see that, although the linearization performance is slightly worse than that of BO-DPD, with the 2-target DPD, the signals at the two target directions, y_1, y_2, are effectively

TABLE I
ACPR AND NMSE FOR RECEIVED SIGNALS

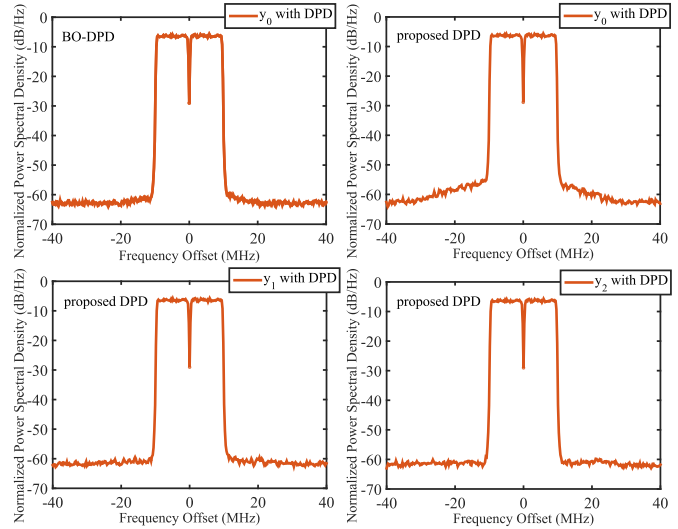| DPD techniques	Rx signals	ACPR(dBc)	NMSE(dB)
BO-DPD	y_0 (0°)	-57.5/-57.3	-48.1
Proposed DPD, $\delta = -25.6$ dB	y_1 (−13°)	-54.9/-54.7	-45.6
	y_2 (+13°)	-54.7/-54.0	-44.7
	y_0 (0°)	-53.2/-54.4	-38.7

Fig. 10. PSDs of the main beam signal with BO-DPD, the main beam and two target signals with the proposed DPD.
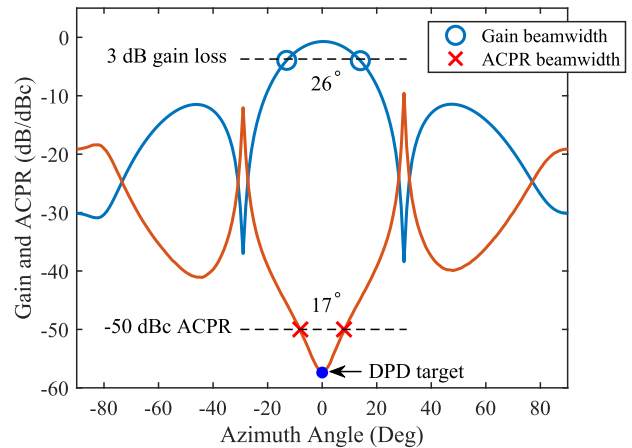

Fig. 11. Gain and ACPR distribution of BO-DPD oriented at 0°.

linearized, and the nonlinearity of the main beam signal y_0 is also effectively removed, e.g., ACPR < -50 dBc.

To illustrate the beamwidth extension, we plot the gain and ACPR distribution verse the Azimuth angle for BO-DPD and the proposed DPD in Figs. 11 and 12, respectively. As shown in Fig. 11, with BO-DPD, the ACPR curve is sharper than the gain curve. If we use −50 dBc as the threshold, the ACPR beamwidth is only 17° while the gain beamwidth is 26° if the 3-dB gain loss is considered. With the proposed DPD,
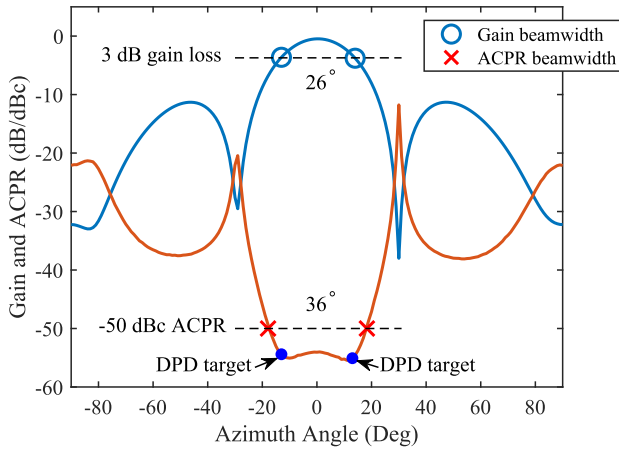
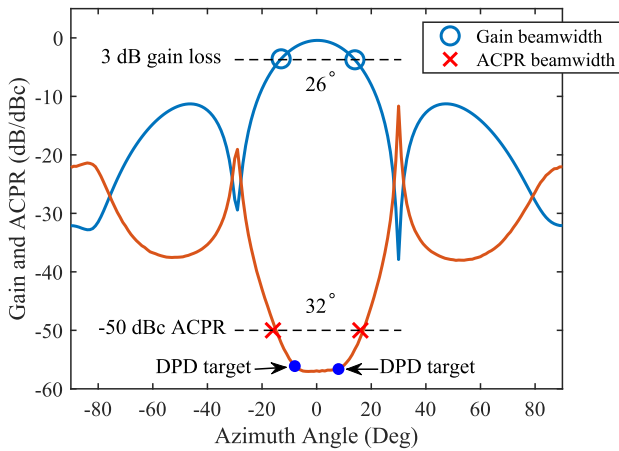Fig. 12.　Gain and ACPR distribution with the proposed DPD, with $\delta = -25.6$ dB, target angles $\pm13°$.

Fig. 13.　Gain and ACPR distribution with the proposed DPD, with $\delta = -25.6$ dB, target angles $\pm8°$.

Fig. 14.　(a) Transmitting performance without DPD and with BO-DPD. (b) Transmitting performance with the proposed DPD, targets $\pm8°$.

TABLE II
POWER AND PAPR FOR THE DPD SIGNALS

Signals	Targets	$\delta = -25.6$ dB		$\delta = -19$ dB	
		Power[a]	PAPR[a]	Power	PAPR
x_1	$\pm13°$	-6.33	7.01	-6.33	6.99
δx_2		-34.86	5.85	-26.78	5.06
x_1	$\pm8°$	-6.28	7.08	-6.3	7.07
δx_2		-34.66	6.53	-26.88	4.89

[a] Power and PAPR values here are all given in dB, and the power values are all normalized according to x_1 in each scenario.

the ACPR beamwidth is widened to 36°, while the gain curve is almost kept the same, as shown in Fig. 12.

To check the impact of the selection of DPD targets, we conducted another simulation with the DPD reference signals captured at $\pm8°$ directions. The results are shown in Fig. 13, where we can see that the ACPR beamwidth becomes narrower, namely, reduced to 32°, but in this case, linearity is flatter within the range, i.e., the ripple is smaller. This indicates that, in real applications, there are some trade-offs that can be made.

Fig. 14 shows the OOB emissions before and after DPD. The OOB emission pattern in the main-beam range is improved by BO-DPD but in a narrow-nulling way. With the proposed DPD, the in-band power pattern is kept and the OOB emission pattern has two lower points at the target angles $\pm8°$ and the linearization angle is thus widened effectively.

B. DPD Signal Characteristics

The power and peak to average power ratio (PAPR) of DPD output signals x_1 and x_2 are given with two different auxiliary attenuation values in Table II when target angles
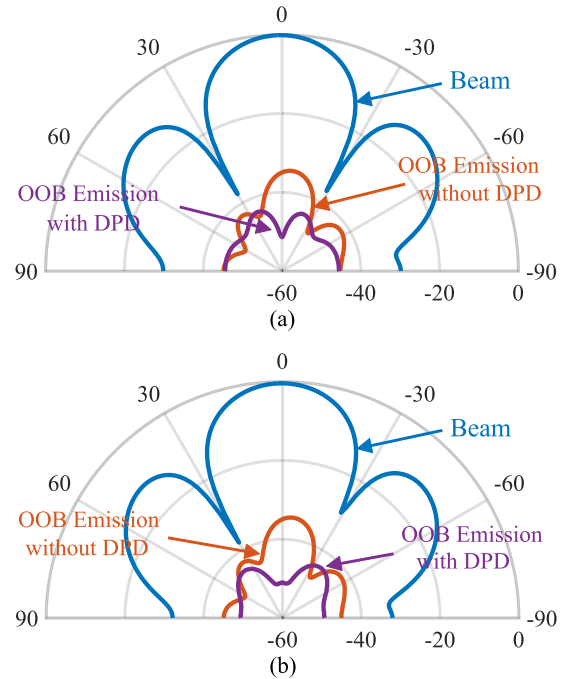
are $\pm13°$ and $\pm8°$. Note that the x_2 is given after it passes the digital attenuator, to show the output power of the digital end. It can be found that the main DPD block output x_1 does not change much in either power or PAPR when different angle targets are used. The power and PAPR of the auxiliary DPD output x_2 are affected by the attenuation factor δ. In general, significant reduction in power is achieved with the auxiliary DPD attenuation.

The PSDs of the DPD signals under different attenuation values and target angles are given in Fig. 15. The PSDs of x_1 look alike but the in-band power of x_2 looks more suppressed with $\delta = -25.6$ dB, with the OOB nonlinearity basically at the same level in x_2. There is something in common, which is the nonlinearity the auxiliary DPD provides.

C. Impact of Attenuation Factor

To exploit the appropriate auxiliary attenuation factor δ, different attenuation values were simulated for the proposed
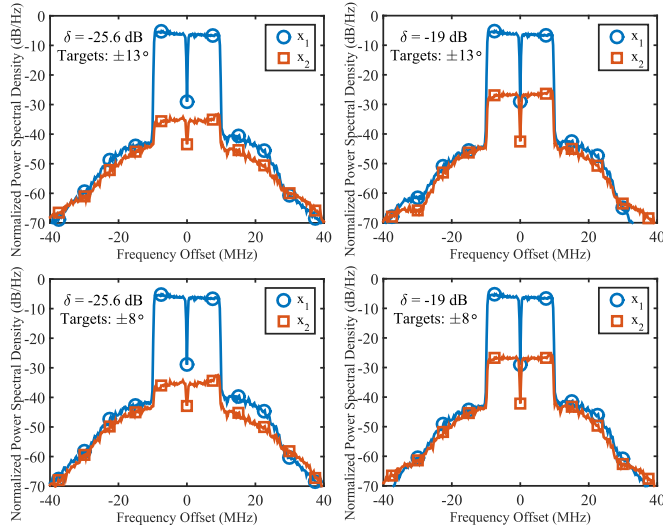
Fig. 15. PSDs of DPD output signals with the proposed DPD.

TABLE III
AUXILIARY DPD SIGNALS WITH DIFFERENT ATTENUATION

| δ | δ(dB) | δx_2 (dB) | | | ACPR |
		Max	Power	PAPR	beamwidth
1/69	-36.8	-20.00	-36.32	16.32	22°
1/59	-35.4	-20.45	-37.07	16.62	29°
1/49	-33.8	-20.92	-38.53	17.61	32°
1/39	-31.8	-21.72	-38.55	16.83	32°
1/29	-29.2	-23.10	-38.28	15.18	32°
1/19	-25.6	-28.13	-34.66	6.53	32°
1/9	-19.0	-21.99	-26.88	4.89	31°
1/3	-9.5	-10.96	-16.69	5.73	25°
1	0	-0.34	-6.56	6.22	16°

DPD with target angles ±8°. The results of auxiliary DPD output x_2 and the ACPR beamwidths are given in Table III.

Observing the power values, the proposed DPD is found to be able to compensate for the excessive attenuation during the DPD extraction, e.g., when $1/59 \leq \delta \leq 1/39$. But too small δ still damages the proposed DPD because of bad extraction accuracy. The DPD performance is weakened by too large δ because too strong inter-modulation will invalidate the DI-DPD models used in the extraction. It also refers to the maximum of δx_2. Concerning both limits, −29.2 or −25.6 dB is an appropriate value for the attenuator δ in this simulation.

The DPD performance and DPD output signals with abnormal δ are illustrated in Figs. 16 and 17. The original array pattern is affected by $\delta = 0$ dB, and the linearization angle is not widened due to not proper nonlinearity provided by δx_2 with relatively too small $\delta = -36.8$ dB.

D. Antenna Crosstalk and Beam Steering Robustness

In beamforming transmitters, crosstalk may occur between antennas or RF chains that can deteriorate linearization performance. To validate the proposed DPD in the scenarios with crosstalk, crosstalk functions were added with random coefficients and real-measured S-parameters to form the dual-input
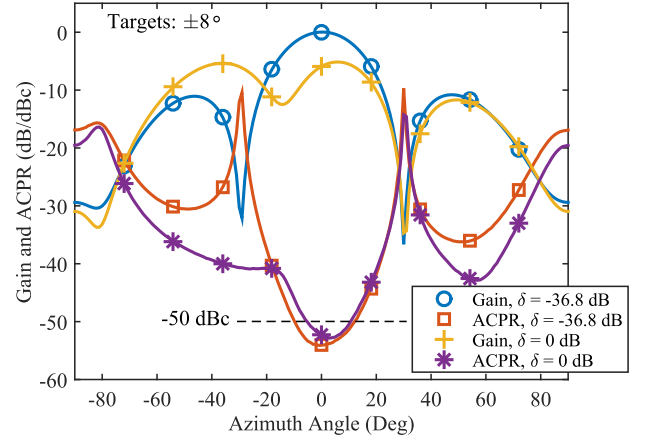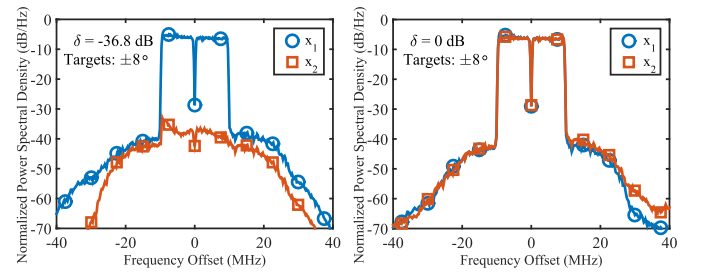

Fig. 16. Gain and ACPR distribution with the proposed DPD, $\delta = -36.8$ dB or $\delta = 0$ dB, target angles ±8°.

Fig. 17. PSDs of DPD output signals of the proposed DPD, $\delta = -36.8$ dB or $\delta = 0$ dB, target angles ±8°.

TABLE IV
ACPR AND NMSE FOR RECEIVED SIGNALS WITH ANTENNA CROSSTALK

DPD techniques	Rx signals	ACPR(dBc)	NMSE(dB)
BO-DPD	y_0 (0°)	-57.4/-56.9	-47.9
Proposed DPD, $\delta = -25.6$ dB	y_1 (−8°)	-56.9/-56.7	-44.4
	y_2 (+8°)	-56.6/-56.5	-47.9
	y_0 (0°)	-55.7/-57.1	-44.8

models used in [11]. The crosstalk strength was controlled to be moderate, making a 3.5-dB ACPR loss in the main-beam direction using the original BO-DPD coefficients.

Both BO-DPD and the proposed DPD were simulated after crosstalk added, the ACPR and NMSE of the received signals with DPDs are given in Table IV. Compared with Table I, the linearization precision for both DPDs does not change much. As shown in Fig. 18, the ACPR beamwidth is 15° with BO-DPD, 30° with the proposed DPD, respectively. This indicates that the 2-target DPD works well when crosstalk occurs.

Antenna crosstalk is usually beam angle-dependent which leads that the system linearity is different at different steering angles. To validate this case, we steered the beam angle from 0° to 30° with the original DPD coefficients fixed. The results are shown in Fig. 18, where we can see that linearity deteriorates in both cases with BO-DPD and the proposed DPD, but the ACPR beamwidth can still be kept wide, e.g., 40° with the proposed DPD, which means that the proposed DPD works well with crosstalk in beam steering.
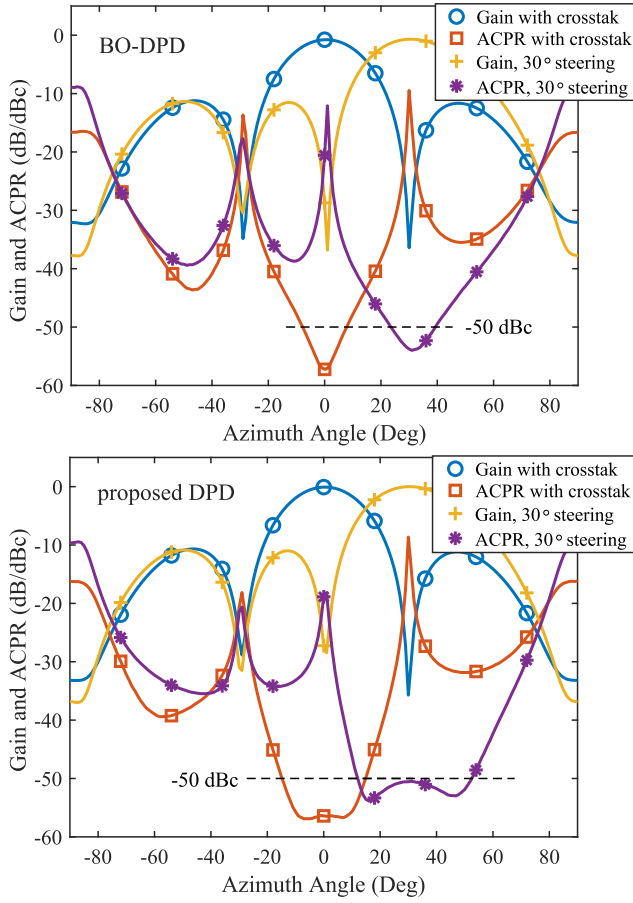
Fig. 18. Gain and ACPR distribution of the proposed DPD oriented at ±8°, and BO-DPD in the 4-path simulation with nonlinear antenna crosstalk.

TABLE V

ACPR AND NMSE FOR RECEIVED SIGNALS IN MASSIVE MIMO (mMIMO) SCENARIOS

Array scenarios	Rx signals	ACPR(dBc)	NMSE(dB)
8-Path $\delta = -25.6\,\text{dB}$	$y_1(-4°)$	-56.7/-57.0	-46.1
	$y_2\,(+4°)$	-56.9/-57.2	-48.2
	$y_0\,(0°)$	-58.0/-58.2	-49.8
16-Path $\delta = -25.6\,\text{dB}$	$y_1\,(-2.5°)$	-56.2/-56.0	-46.4
	$y_2\,(+2.5°)$	-56.5/-56.3	-47.9
	$y_0\,(0°)$	-58.0/-57.9	-49.8

E. Large Scale Validations

To verify how the proposed DPD performs in large-scale beamforming transmitters, e.g., mMIMO, we simulated the 8- and 16-path transmitters. The results of y_1, y_2, and y_0 with the target angles at ±4° and ±2.5° are given in Table V, where we can see that the DPD works very well. The gain and ACPR curves are illustrated in Fig. 19, where the ACPR bandwidth is 20° and 10° for 8- and 16-path, respectively. Furthermore, the ACPR curves are greatly improved to be such as a mirror image of the gain curves, which indicates that the proposed DPD even performs better in mMIMO transmitters than in small-scale array systems because we not only can extend the linearization angle but also effectively match the linearity
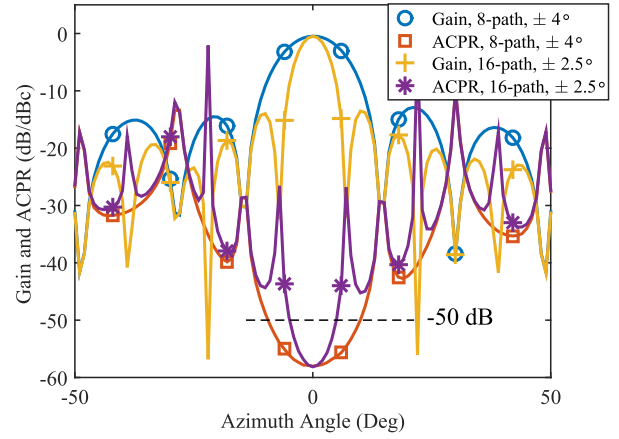

Fig. 19. Gain and ACPR distribution of the simulated 8- and 16-path transmitters with the proposed DPD, target angles ±4° or ±2.5°.

TABLE VI

DPD RUNNING COMPLEXITY

DPD techniques	Number of coefficients	$K = 16$
BO-DPD	$(P+1)(M_1+1)(M_2+1)/2$	48
Proposed DPD	$(P+1)(M_1+1)(M_2+1)$	96
Full-angle DPD	$(P+1)(M_1+1)(M_2+1)/2$ $+(K-1)(P_t+1)(M_t+1)/2$	138
Multiple-DPD	$K(P+1)(M_1+1)(M_2+1)/2$	768

with the gain characteristics, which improve the overall system performance.

F. Complexity Analysis

The proposed DPD, BO-DPD, full-angle DPD, and the multiple-DPD are analyzed for complexity comparison. Two complexities are evaluated: running complexity and model extraction complexity.

Running complexity is related to the operations that the DPD modules process the real-time data, e.g., in the main and auxiliary DPD blocks. To be fair, the basis functions are all based on the GMP model. Since the running complexity is in proportion to the number of DPD coefficients used, Table VI shows the number of DPD coefficients varying with the nonlinear order P, the memory depth M_1, M_2, the number of paths K, the tuning-box nonlinear order P_t, and the tuning-box memory depth M_t, e.g., $P = 7$, $M_1 = 5$, $M_2 = 1$, $P_t = 5$, $M_t = 1$ used in the simulation and experiment. The complexities of BO-DPD and the proposed DPD do not depend on K. Multiple-DPD has the highest complexity which is proportional to K. Full-angle DPD and the proposed DPD have medium complexities. The proposed DPD has the advantage in the complexity for mMIMO systems, e.g., when $K = 16$. To reduce the running complexity further, once the main and auxiliary DPD blocks are determined, simpler models could be used to remodel the DPD functions, e.g., memory polynomial (MP) model. And the two blocks have the same basic functions and the same input, the calculation resource can be much reduced in deployment.

Extraction complexity is proportional to the cubic of the number of polynomial coefficients used in the DI-DPD blocks
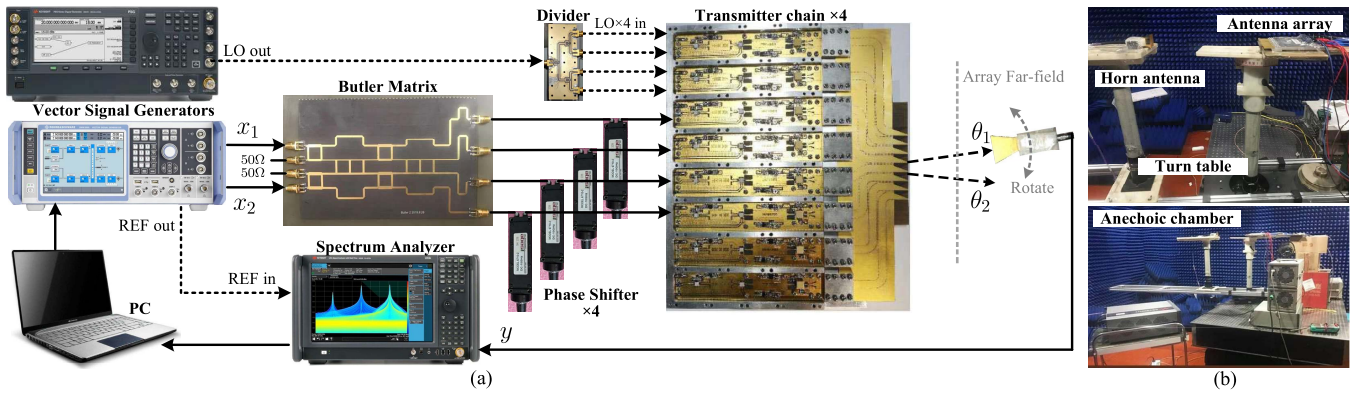
Fig. 20.   (a) Test bench setup for the 2×4 analog beamforming application. (b) Test bench setup.

extraction if the least squares (LSs) method is employed. The extraction complexity of the proposed DPD is relatively higher than that of BO-DPD. This would not be an issue since the DPD extraction process is for an initial DPD identification for once. In real-time operation, more effective adaptive algorithms can be used [8]. In addition, to reduce the extraction complexity, further pruned bivariate models can be employed.

V. EXPERIMENTAL RESULTS

In this section, the measurement setups are illustrated, to validate the proposed DPD technique applied to beamforming systems. The results, related comparisons, and analysis are presented to evaluate the DPD performance.

A. Measurement Setup

The analog beamforming setup includes a 4×4 Butler matrix and four analog phase shifters. Fig. 20(a) shows a diagram of the test bench including photographs of the Butler matrix, four PA-antenna transmitter chains, the antenna array, and related instruments. Fig. 20(b) shows the photos of the real test bench setup in the anechoic chamber.

Two uncorrelated and independent OFDM signals were generated by the software MATLAB, downloaded to vector signal generators, and then up-converted to 5.5 GHz, as the intermediate frequency (IF) signals. The bandwidth of signals is 20 MHz, the sampling rate is 120 MHz and the PAPRs are 5.69 and 5.63 dB respectively. A dual-channel vector signal generator (R&S, SMW200A) was used to generate the two IF signals, and two channels were synchronized with the local-oscillator (LO) option, using the same LO. The two IF signals were distributed to four IF signals through a 4×4 Butler matrix, which is designed to distribute the main signal x_1 from the front-end port 1 to the four back-end ports with the phase difference $0°$, and transmit the auxiliary signal x_2 from the front port 4 to the four backports with a $90°$ progressive phase increase relative to the preceding one. In this test, the array spacing is 6 mm, slightly longer than the half-wavelength 5.5 mm at 27 GHz. And the left front port 2 and port 3 were matched with standard $50\,\Omega$ load.

The two test scenarios for BO-DPD and the proposed DPD were switched manually by adding the Butler matrix and operating the calibration again. Each pair of Butler matrix back output and transmitter chain were connected with a

TABLE VII
ACPR AND NMSE FOR RECEIVED SIGNALS WITH AND WITHOUT DPDS

DPD techniques	Rx signals	ACPR(dBc)	NMSE(dB)
w/o DPD	y_0 $(0°)$	-34.6/-34.0	-18.2
BO-DPD	y_0 $(0°)$	-56.8/-56.2	-42.8
Proposed DPD, $\delta = -20\,\text{dB}$	y_1 $(+8°)$	-55.8/-56.2	-43
	y_2 $(-8°)$	-56.5/-56.3	-42.5
	y_0 $(0°)$	-54.9/-52.4	-40.3

phase shifter, to adjust the phase shifting caused by the length inconsistency of the millimeter-wave chains, and to form the proper beam pattern. The phase shifters were manually calibrated in pairs. In calibration, path 1 was turned on and its phase shifting value was kept fixed. Among the other paths, only path k was turned on to adjust the phase shifter k to steer the beam at $0°$.

Besides, the 10.75-GHz LO signal was generated by the signal generator (Keysight E8267D), divided into four LO signals for the four chains. And the error of the four LO coaxial lines was customized to be less than $3°$ in phase. The Class-AB PAs operated at 27 GHz had about 14-dBm output power, and were connected to a tapered slot antenna array directly. The mutual coupling of adjacent antenna units is less than -23 dB. After about 50 cm of spatial propagation, the far-field OTA signals were received by a standard horn fixed on a turntable, then transmitted to a spectrum analyzer (Keysight, N9030A). The proposed DPD and others were all applied with $P = 7$, $M_1 = 5$, $M_2 = 1$ as the same models used in simulations, and the results were given after three iterations. The attenuation δ for the auxiliary digital path in the proposed method was set -20 dB.

B. Performance of the DPDs in 4-Path Scenarios

The ACPR and NMSE of OTA received signals were measured to evaluate the performances of conventional BO-DPD and the proposed DPD, as given in Table VII. y_0 is the beam signal, y_1, y_2 are the two linearization target signals, as shown in Fig. 8. Both DPDs improved beam signal from around -34 to below -50 dBc in ACPR, from -18 to below -40 dB in NMSE. The proposed DPD improved the two received signals at the target angles to the same level of beam signal in BO-DPD, at around -56-dBc ACPR and -43-dB NMSE.
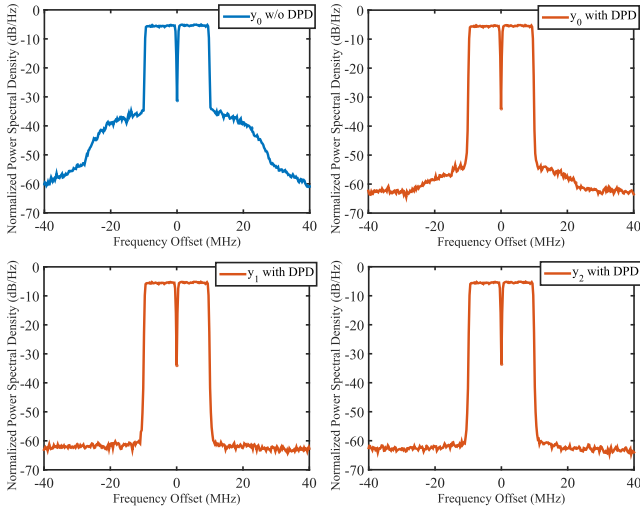
Fig. 21. PSDs of the main beam signal without/with the proposed DPD, and linearization target signals with the proposed DPD, targets $\pm 8°$.
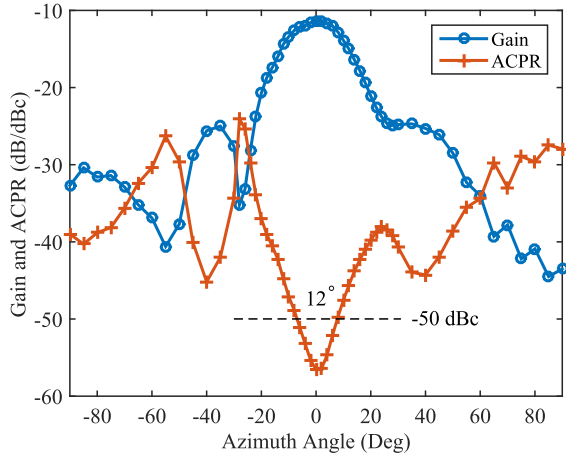

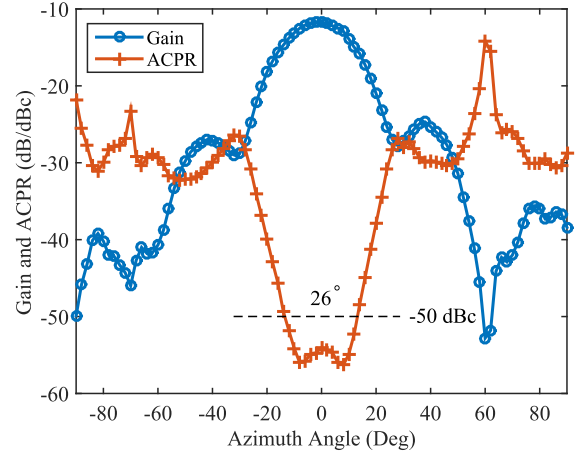Fig. 22. Normalized gain and ACPR distribution with BO-DPD.

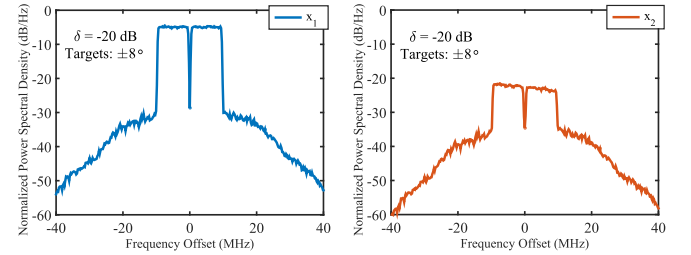Fig. 23. Normalized gain and ACPR distribution with the proposed DPD.

Fig. 24. Normalized PSDs of DPD signals with the proposed DPD.

TABLE VIII
POWER AND PAPR FOR DPD SIGNALS

DPD signals	Power (dBm)		PAPR(dB)	
	Initial	With DPD	Initial	With DPD
x_1	12.50	13.08	5.69	7.41
δx_2	-7.44	-4.31	5.63	11.00

Fig. 21 shows the normalized PSD for original signal of y_0, noted as w/o DPD, and y_0, y_1, and y_2 with the proposed DPD. The OOB distortion is removed for the two linearization targets and the nonlinearity of beam signal y_0 is acceptable.

Fig. 22 shows the results of normalized gain and ACPR distribution with the BO-DPD, where the beam is at $0°$. The ACPR beamwidth under -50 dBc is $12°$.

Fig. 23 shows results of the normalized gain and ACPR distribution on the Azimuth angle with the proposed DPD, where the beam is at $0°$, and the target angles are $\pm 8°$. The ACPR beamwidth under -50 dBc is $26°$ and basically symmetrical.

Comparing the ACPR results, the proposed DPD improved the ACPR beamwidth under -50 dBc from $12°$ with BO-DPD to $26°$. The proposed linearization angle widening method is validated. Comparing the normalized gain results, the proposed DPD did not change the radiation pattern basically in the main beam range, as designed in the proposed DPD. Although the peak gain and directions of sidelobes are similar, the pattern of the sidelobes could be found obviously different. It is due to the dismantlement of the Butler matrix and re-calibration of the phase shifters when the test setup was changed from the proposed DPD state to the BO-DPD state.

The PSDs of DPD outputs x_1, x_2 are given in Fig. 24, where the OOB nonlinear parts of x_1, x_2 look alike and they have similar power levels. While the power requirement of x_2 was significantly reduced by the attenuator design.

The output power of x_1, δx_2, and their PAPRs without or with the proposed DPD are given as Table VIII. Concerning the power variation of x_2, compared with the simulation, the convergence power is a little bigger than the initial power, rather than a little smaller. It should depend on the PA inconsistency in the simulation and experiment.

C. Asymmetrical Linearization Targets

The normalized gain and ACPR of the OTA received signals after BO-DPD, and the proposed DPD with asymmetrical targets, are given as Fig. 25 for comparison. The results with the proposed DPD are denoted as linearization angle widen (LAW) DPD. The target angles are $-14°$ and $6°$, and the ACPR beamwidth under -50 dBc is improved from $12°$ with BO-DPD to $26.5°$ (from $-16°$ to $10.5°$). This validates that the asymmetrical linearization-target configuration is applicable for the proposed DPD. Not only the number but also the angle of linearization targets will change the ACPR distribution in the main beam range.
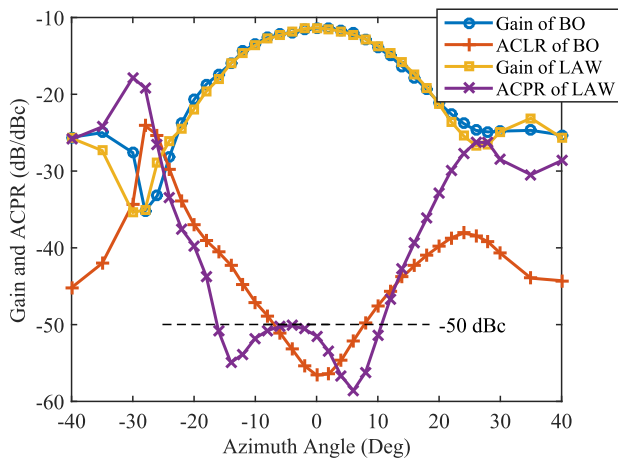
Fig. 25. Normalized gain and ACPR distribution with the proposed DPD (target angles −14° and 6°) and BO-DPD.

The two gain curves basically coincide with each other, which validates the array pattern of the proposed DPD, especially in the main beam range.

VI. Conclusion

In this article, a novel 2-target DPD solution is given as an example of the proposed multi-target DPD to widen the ACPR beamwidth for MIMO transmitters. A low-power auxiliary DPD block is added to the conventional DPD structure to shape the pattern of nonlinear distortion without changing the original radiation pattern. To apply ILA in the model extraction, a new DPD model extraction architecture including OTA signals post-processing is carefully designed. According to the simulation and experimental results, the proposed 2-target DPD method can realize good linearity within a wider angle range, compared with the BO-DPD method. The results indicate that the proposed DPD has the advantage of scaling to mMIMO systems, which is promising in 5G MIMO transmitters.

References

[1] M. Shafi *et al.*, "5G: A tutorial overview of standards, trials, challenges, deployment, and practice," *IEEE J. Sel. Areas Commun.*, vol. 35, no. 6, pp. 1201–1221, Jun. 2017.

[2] H. Yan, S. Ramesh, T. Gallagher, C. Ling, and D. Cabric, "Performance, power, and area design trade-offs in millimeter-wave transmitter beamforming architectures," *IEEE Circuits Syst. Mag.*, vol. 19, no. 2, pp. 33–58, May 2019.

[3] L. Guan and A. Zhu, "Green communications: Digital predistortion for wideband RF power amplifiers," *IEEE Microw. Mag.*, vol. 15, no. 7, pp. 84–99, Nov./Dec. 2014.

[4] J. Wood, "System-level design considerations for digital pre-distortion of wireless base station transmitters," *IEEE Trans. Microw. Theory Techn.*, vol. 65, no. 5, pp. 1880–1890, May 2017.

[5] Q. Luo, C. Yu, and X.-W. Zhu, "Digital predistortion of phased array transmitters with multi-channel time delay," in *Proc. IEEE Topical Conf. RF/Microw. Power Model. Radio Wireless Appl. (PAWR)*, Jan. 2018, pp. 54–57.

[6] C. Fager, T. Eriksson, F. Barradas, K. Hausmair, T. Cunha, and J. C. Pedro, "Linearity and efficiency in 5G transmitters: New techniques for analyzing efficiency, linearity, and linearization in a 5G active antenna transmitter context," *IEEE Microw. Mag.*, vol. 20, no. 5, pp. 35–49, May 2019.

[7] F. M. Barradas, P. M. Tomé, J. M. Gomes, T. R. Cunha, P. M. Cabral, and J. C. Pedro, "Power, linearity, and efficiency prediction for MIMO arrays with antenna coupling," *IEEE Trans. Microw. Theory Techn.*, vol. 65, no. 12, pp. 5284–5297, Dec. 2017.

[8] K. Hausmair, P. N. Landin, U. Gustavsson, C. Fager, and T. Eriksson, "Digital predistortion for multi-antenna transmitters affected by antenna crosstalk," *IEEE Trans. Microw. Theory Techn.*, vol. 66, no. 3, pp. 1524–1535, Mar. 2018.

[9] Q. Luo, C. Yu, and X.-W. Zhu, "A dual-input canonical piecewise-linear function-based model for digital predistortion of multi-antenna transmitters," in *IEEE MTT-S Int. Microw. Symp. Dig.*, Jun. 2018, pp. 559–562.

[10] P. Jaraut, M. Rawat, and F. M. Ghannouchi, "Composite neural network digital predistortion model for joint mitigation of crosstalk, I/Q imbalance, nonlinearity in MIMO transmitters," *IEEE Trans. Microw. Theory Techn.*, vol. 66, no. 11, pp. 5011–5020, Nov. 2018.

[11] Q. Luo, X. Zhu, C. Yu, and W. Hong, "Single-receiver over-the-air digital predistortion for massive MIMO transmitters with antenna crosstalk," *IEEE Trans. Microw. Theory Techn.*, vol. 68, no. 1, pp. 301–315, Jan. 2020.

[12] X. Wang, Y. Li, C. Yu, W. Hong, and A. Zhu, "Digital predistortion of 5G massive MIMO wireless transmitters based on indirect identification of power amplifier behavior with OTA tests," *IEEE Trans. Microw. Theory Techn.*, vol. 68, no. 1, pp. 316–328, Jan. 2020.

[13] N. Tervo, J. Aikio, T. Tuovinen, T. Rahkonen, and A. Parssinen, "Digital predistortion of amplitude varying phased array utilising over-the-air combining," in *IEEE MTT-S Int. Microw. Symp. Dig.*, Jun. 2017, pp. 1165–1168.

[14] X. Liu *et al.*, "Beam-oriented digital predistortion for 5G massive MIMO hybrid beamforming transmitters," *IEEE Trans. Microw. Theory Techn.*, vol. 66, no. 7, pp. 3419–3432, Jul. 2018.

[15] C. Yu *et al.*, "Full-angle digital predistortion of 5G millimeter-wave massive MIMO transmitters," *IEEE Trans. Microw. Theory Techn.*, vol. 67, no. 7, pp. 2847–2860, Jul. 2019.

[16] E. Ng, Y. Beltagy, P. Mitran, and S. Boumaiza, "Single-input single-output digital predistortion of power amplifier arrays in millimeter wave RF beamforming transmitters," in *IEEE MTT-S Int. Microw. Symp. Dig.*, Jun. 2018, pp. 481–484.

[17] M. Abdelaziz, L. Antilla, A. Brihuega, F. Tufvesson, and M. Valkama, "Digital predistortion for hybrid MIMO transmitters," *IEEE J. Sel. Topics Signal Process.*, vol. 12, no. 3, pp. 445–454, Jun. 2018.

[18] A. Ghosh, A. Maeder, M. Baker, and D. Chandramouli, "5G evolution: A view on 5G cellular technology beyond 3GPP release 15," *IEEE Access*, vol. 7, pp. 127639–127651, 2019.

[19] A. Tajik, A. S. Alavijeh, and M. Fakharzadeh, "Asymmetrical 4 × 4 butler matrix and its application for single layer 8 × 8 butler matrix," *IEEE Trans. Antennas Propag.*, vol. 67, no. 8, pp. 5372–5379, Aug. 2019.

[20] J. Jing and C. Yu, "Multibeam digital predistortion for millimeter-wave analog beamforming transmitters," *IEEE Microw. Wireless Compon. Lett.*, vol. 30, no. 2, pp. 209–212, Feb. 2020.

[21] X. Liu, W. Chen, L. Chen, and Z. Feng, "Beam-oriented digital predistortion for hybrid beamforming array utilizing over-the-air diversity feedbacks," in *IEEE MTT-S Int. Microw. Symp. Dig.*, Jun. 2019, pp. 987–990.

[22] S. Lee *et al.*, "Digital predistortion for power amplifiers in hybrid MIMO systems with antenna subarrays," in *Proc. IEEE 81st Veh. Technol. Conf. (VTC Spring)*, May 2015, pp. 1–5.

[23] R. Murugesu, M. Holyoak, H. Chow, and S. Shahramian, "Linearization of mm-wave large-scale phased arrays using near-field coupling feedback for >10Gb/s wireless communication," in *IEEE MTT-S Int. Microw. Symp. Dig.*, Aug. 2020, pp. 1271–1274.

[24] S. Hesami, S. R. Aghdam, J. Dooley, T. Eriksson, and C. Fager, "Amplitude varying phased array linearization," in *Proc. IEEE Eur. Microw. Conf. (EuMC)*, Jan. 2021, pp. 348–351.

[25] N. Tervo *et al.*, "Digital predistortion of phased-array transmitter with shared feedback and far-field calibration," *IEEE Trans. Microw. Theory Techn.*, vol. 69, no. 1, pp. 1000–1015, Jan. 2021.

[26] D. Rönnow, "pth-order inverse of the volterra series for multiple-input multiple-output non-linear dynamic systems," *IET Circuits, Devices Syst.*, vol. 12, no. 4, pp. 403–412, Jul. 2018.

[27] S. Amin, P. Landin, P. Händel, and D. Rönnow, "Behavioral modeling and linearization of crosstalk and memory effects in RF MIMO transmitters," *IEEE Trans. Microw. Theory Techn.*, vol. 62, no. 4, pp. 810–823, Apr. 2014.

[28] D. R. Morgan, Z. Ma, J. Kim, M. G. Zierdt, and J. Pastalan, "A generalized memory polynomial model for digital predistortion of RF power amplifiers," *IEEE Trans. Signal Process.*, vol. 54, no. 10, pp. 3852–3860, Oct. 2006.

Qing Luo (Graduate Student Member, IEEE) was born in Yangzhou, Jiangsu, China, in 1992. He received the B.E. degree in information engineering from Southeast University (SEU), Nanjing, China, in 2014, where he is currently pursuing the Ph.D. degree in electromagnetic field and microwave technology at the State Key Laboratory of Millimeter Waves.

His current research interests include modeling and linearization for RF power amplifiers and multiple-input-multiple-output (MIMO) RF systems.

Xiao-Wei Zhu (Member, IEEE) received the M.E. and Ph.D. degrees in radio engineering from Southeast University, Nanjing, China, in 1996 and 2000, respectively.

Since 1984, he has been with Southeast University, where he is currently a Professor with the School of Information Science and Engineering. He has authored or coauthored over 100 technical publications. He holds over 20 patents. His research interests include RF and antenna technologies for wireless communications, microwave and millimeter-wave theory and technology, and power amplifier (PA) nonlinear character and its linearization research with a particular emphasis on wideband and high-efficiency GaN PAs.

Dr. Zhu is on the Microwave Society of the Chinese Institute of Electronics (CIE), and the Secretary of the IEEE MTT-S/AP-S/EMC-S Joint Nanjing Chapter. He was a recipient of the 2003 Second-Class Science and Technology Progress Prize of Jiangsu Province, China.

Chao Yu (Senior Member, IEEE) received the B.E. degree in information engineering and the M.E. degree in electromagnetic fields and microwave technology from Southeast University (SEU), Nanjing, China, in 2007 and 2010, respectively, and the Ph.D. degree in electronic engineering from the University College Dublin (UCD), Dublin, Ireland, in 2014.

He is currently a Professor with the State Key Laboratory of Millimeter Waves, School of Information Science and Engineering, SEU, and Purple Mountain Laboratories, Nanjing. His current research interests include microwave and millimeter wave power amplifier modeling and linearization and 5G massive multiple-input-multiple-output (MIMO) RF system design.

Dan-Dan Teng (Student Member, IEEE) was born in Weihai, China, in 1995. She received the B.E. degree in electronic information science and technology from Southwest Jiaotong University (SWJTU), Chengdu, China, in 2018. She is currently pursuing the M.S. degree in electromagnetic field and microwave technology at Southeast University (SEU), Nanjing, China.

Her current research interests include digital predistortion for RF power amplifiers and multi-antenna transmitters.

Xiaoyu Wang (Graduate Student Member, IEEE) received the B.E. degree in information engineering from Southeast University, Nanjing, China, in 2015. She is currently pursuing the Ph.D. degree at the University College Dublin (UCD), Dublin, Ireland.

She is also with the RF and Microwave Research Group, UCD. Her current research interests include digital predistortion for RF power amplifiers, with a particular emphasis on applications to multiple-input multiple-output (MIMO) systems.

Chenhao Chu (Graduate Student Member, IEEE) received the B.E. degree from the Nanjing University of Science and Technology, Nanjing, China, in 2015, and the M.S. degree (Hons.) from the City University of Hong Kong, Hong Kong, SAR, China, in 2017. He is currently pursuing the Ph.D. degree at the RF and Microwave Research Group, University College Dublin, Dublin, Ireland.

From October 2017 to September 2018, he was a Research Assistant with the State Key Laboratory of Millimeter Waves, Department of Electronic Engineering, City University of Hong Kong. His research interests include broadband high-efficiency power amplifiers, MMIC power amplifier design for RF/microwave and millimeter-wave applications, and antenna-in-package at mm-Waves.


Wei Hong (Fellow, IEEE) received the B.S. degree from the University of Information Engineering, Zhengzhou, China, in 1982, and the M.S. and Ph.D. degrees from Southeast University, Nanjing, China, in 1985 and 1988, respectively, all in radio engineering.

Since 1988, he has been with the State Key Laboratory of Millimeter Waves and serves for the Director of the Lab since 2003. He is currently a Professor and the Dean of the School of Information Science and Engineering, Southeast University. In 1993, 1995, 1996, 1997, and 1998, he was a short-term Visiting Scholar with the University of California at Berkeley, Berkeley, CA, USA, and the University of California at Santa Cruz, Santa Cruz, CA, respectively. He has been involved in numerical methods for electromagnetic problems, millimeter wave theory and technology, antennas, and RF technology for wireless communications. He has authored and coauthored over 300 technical publications with over 9000 citations, and authored two books.

Dr. Hong was an elected IEEE MTT-S AdCom Member from 2014 to 2016. He is also a Fellow of the Chinese Institute of Electronics (CIE), the Vice President of the CIE Microwave Society and Antenna Society, and the Chair of the IEEE MTT-S/AP-S/EMC-S Joint Nanjing Chapter. He was twice awarded the National Natural Prizes, thrice awarded the First-Class Science and Technology Progress Prizes issued by the Ministry of Education of China and Jiangsu Province Government, and so on. Besides, he received the Foundations for China Distinguished Young Investigators and for "Innovation Group" issued by NSF of China. He has served as an Associate Editor for the IEEE TRANSACTIONS ON MICROWAVE THEORY AND TECHNIQUES from 2007 to 2010, and one of the Guest Editors for the 5G Special Issue of IEEE TRANSACTIONS ON ANTENNAS AND PROPAGATION (AP) in 2017.
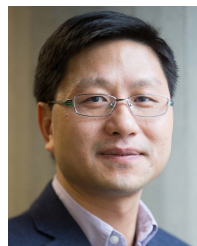
Anding Zhu (Senior Member, IEEE) received the Ph.D. degree in electronic engineering from the University College Dublin (UCD), Dublin, Ireland, in 2004.

He is currently a Professor with the School of Electrical and Electronic Engineering, UCD. He has authored more than 150 peer-reviewed journal articles and conference papers. His research interests include high-frequency nonlinear system modeling and device characterization techniques, high-efficiency power amplifier design, wireless transmitter architectures, digital signal processing, and nonlinear system identification algorithms.

Prof. Zhu is also an Elected Member of MTT-S AdCom, the Chair of the Electronic Information Committee, and the Vice Chair of the Publications Committee. He is also the Chair of the MTT-S Microwave High-Power Techniques Committee. He has served as the Secretary for MTT-S AdCom in 2018. He was the General Chair of the 2018 IEEE MTT-S International Microwave Workshop Series on 5G Hardware and System Technologies (IMWS-5G) and a Guest Editor of the IEEE TRANSACTIONS ON MICROWAVE THEORY AND TECHNIQUES ON 5G HARDWARE AND SYSTEM TECHNOLOGIES. He is also an Associate Editor of *IEEE Microwave Magazine* and a Track Editor of the IEEE TRANSACTIONS ON MICROWAVE THEORY AND TECHNIQUES.